MATERIALS CHEMISTRY
FRONTIERS

CCS 中国化学会 CHINESE CHEMICAL SOCIETY
ICCAS
ROYAL SOCIETY OF CHEMISTRY

RESEARCH ARTICLE

View Article Online
View Journal | View Issue

Cite this: *Mater. Chem. Front.*, 2024, **8**, 274

Excitation-dependent efficient photoluminescence in an organic–inorganic $(C_4H_{12}N)_2HfCl_6$ perovskite induced by antimony doping†

Jingheng Nie,‡[a] Xiangyan Yun,‡[b] Zexiang Liu,[b] Hailin Zhou,[b] Hanlin Hu,[c] Haizhe Zhong,[b] Yumeng Shi *[d] and Henan Li*[d]

Received 15th September 2023,
Accepted 30th October 2023

DOI: 10.1039/d3qm01015e

rsc.li/frontiers-materials

Organic–inorganic lead (Pb)-free halide perovskites exhibit considerable potential as photoluminescence materials because of outstanding photophysical properties. However, metal halide perovskites generally emit single self-trapped excitons at room temperature, making it difficult to achieve a wide color gamut using simple external stimuli. Herein, a novel antimony (Sb)-doped hafnium (Hf(IV))-based metal halide hybrid $(TMA)_2HfCl_6$ (TMA = $C_4H_{12}N$) with efficient and remarkable excitation-dependent luminescence is reported. The prepared $(TMA)_2HfCl_6$ samples exhibit two different types of emissions under varying excitation lengths that originate from free excitons and self-trapped excitons. The emissions range from red to white light and can be tuned through precise control of the excitation wavelength. The Pb-free metal halide $(TMA)_2HfCl_6:Sb^{3+}$ exhibits a high photoluminescence quantum yield of 85.55% upon 365 nm ultraviolet excitation and excellent air stability, which are unique advantages for a light-emitting material. These results provide fundamental insights into the color kinetic features of Sb^{3+} in hybrid metal halides, offering guidance for expanding the application scope of luminescent metal halides.

1 Introduction

Organic–inorganic metal halide perovskites are promising light-emitting materials that have attracted widespread attention because of excellent optical performance.[1–4] The availability of a wide variety of organic ligands and metal centers has resulted in materials with structural diversity and optical tunability, enabling various potential applications.[5–7] Considerable effort has been expended to mitigate the intrinsic toxicity and instability of traditional lead (Pb)-based halide perovskites by replacing Pb with low-toxicity or nontoxic metal ions.[8,9] In this regard, a defect double-perovskite variant $A_2B(IV)X_6$ has emerged in recent years, formed by substituting two Pb^{2+} cations with one tetravalent B(IV) cation (such tin (Sn^{4+}), zirconium (Zr^{4+}), or hafnium (Hf^{4+})).[10–12] This variant has aroused considerable interest because of high designability and tunability. Although these vacancy-ordered perovskite materials typically exhibit broadband photoluminescence (PL) from self-trapped excitons (STEs), the transport and recombination of excitons are severely influenced by B(IV)-related vacancies and exciton–phonon coupling, which makes it difficult to directly tune the intrinsic properties of STEs for achieving multicolor emission.[13,14]

Chemical doping is an effective strategy for tailoring the electronic and optical properties of metal halides.[15–21] For example, antimony (Sb^{3+}) ions with ns^2 electronic configurations can be used to confer superb light-emitting properties to materials, typically including efficient broadband STE emission.[22–27] For these halide perovskite materials, excitons are absolutely confined in isolated polyhedrons with strong quantum confinement, ultimately producing only a single STE emission at room temperature and no emission of high-energy free excitons (FEs). Therefore, very limited regulation of the emission color is possible for these materials. Creating a suitable lattice environment can improve the energy barrier between the FEs and STEs of isolated ns^2 centers and make dual-band emission possible.[28] This special emission mechanism provides a feasible strategy for

[a] *Guangdong Rare Earth Photofunctional Materials Engineering Technology Research Center, School of Chemistry and Environment, Jiaying University, Meizhou, 514015, P. R. China*
[b] *International Collaborative Laboratory of 2D Materials for Optoelectronics Science and Technology of Ministry of Education, Institute of Microscale Optoelectronics, Shenzhen University, Shenzhen 518060, P. R. China*
[c] *Hoffman Institute of Advanced Materials, Shenzhen Polytechnic, Shenzhen 518060, P. R. China*
[d] *School of Electronics and Information Engineering, Shenzhen University, Shenzhen 518060, P. R. China. E-mail: yumeng.shi@szu.edu.cn, henan.li@szu.edu.cn*

† Electronic supplementary information (ESI) available: Crystal structures, bond lengths and angles, XRD pattern, PL spectra, PLQY measurement, PL-temperature correlation map, and DFT calculation results (PDF). See DOI: https://doi.org/10.1039/d3qm01015e

‡ The authors contributed equally to this work.

obtaining excitation-dependent emission, such that the color and brightness of the material luminescence can be easily engineered by tuning the excitation wavelength.[29] Although there have been some reports on controlling the luminescence of perovskite crystals, rational manipulation of multiexciton emission in single perovskite materials remains to be realized.[30,31] The complexity of the intrinsic excitation-dependent emission mechanism has made it challenging to develop novel wavelength-sensitive materials to increase the efficiency of multicolor emission.

Herein, the incorporation of Sb^{3+} ions has been used to realize a high-performance dual-emission hybrid organic–inorganic Hf(IV) metal halide with tunable emission through precise control of the excitation wavelength. This organic–inorganic metal halide $(TMA)_2HfCl_6$:Sb^{3+} is unique in that excitation-dependent colored emissions are produced through two different light-emitting modes. On the basis of time-resolved PL and temperature-dependent steady-state spectra, the intriguing dual emission (490 and 660 nm) is determined to originate from FEs and STEs. The internal light-emission mechanism is also elucidated by performing density functional theory (DFT) calculations. The sample emission depends on the excitation wavelength and is bright white with a CIE of (0.37, 0.36) under 310 nm excitation and bright red with a high PL quantum yield (PLQY) of 85.55% under 365 nm excitation. The results of this study prove the feasibility of using an Sb^{3+} doping strategy to achieve excitation-dependent luminescence in hybrid halides and provide useful insights for developing metal-halide luminescent materials.

2 Experimental section

2.1. Materials

Tetramethylammonium chloride ($C_4H_{12}NCl$, TMAC, 99%) was purchased from Shanghai Acmec Biochemical Co., Ltd. Hafnium(IV) chloride ($HfCl_4$, 99.99%) was purchased from Macklin. Antimonous chloride ($SbCl_3$, 99.99%) was purchased from Aladdin. Hydrochloric acid (HCl, Analytical reagent) and deionized water were purchased from Sinopharm Chemical Reagent Co., Ltd. All chemicals were used directly in their original state after purchase, without the need for further purification.

2.2. Synthesis

$(TMA)_2HfCl_6$ and $(TMA)_2HfCl_6$:xSb^{3+} (x = 0, 0.01, 0.02, 0.03, 0.04, 0.05, 0.06 and 0.07) powders were synthesized by the solution method. First, 2.192 g (20 mmol) TMAC was dissolved in 25 ml HCl, 3.203 g (10 mmol) $HfCl_4$ (2 : 1 molar ratio) was dissolved in 18 ml HCl and 7 ml deionized water, and 2.281 g (10 mmol) $SbCl_3$ was dissolved in 10 ml HCl. Subsequently, magnetons were added to the three glass bottles mentioned above, and the bottles were heated to 60 °C under continuous stirring until a uniform and colorless solution was obtained. After that, the glass bottles containing the transparent solution were placed at room temperature for a period of time. For the $(TMA)_2HfCl_6$ host, 0.75 ml $HfCl_4$ transparent solution was dropped into the 1.5 ml TMAC transparent solution, and the white precipitates were formed. For Sb^{3+} doping samples, the synthetic method is the same as the pristine sample except for the addition of $SbCl_3$ transparent solution. Finally, the white precipitates mentioned above were washed and centrifuged, and then dried at 60 °C for 4.5 hours.

2.3. Characterization

Rietveld structure refinements were performed using GSAS software. The microstructures and element scanning analyses were characterized by the fourth generation high-performance Scanning electron microscope (TESCAN MIRA LMS). The powder X-ray diffraction (PXRD) data were collected by a Bruker, D2 X-ray diffractometer. The optical UV-vis absorption measurements were carried out using a UV-3600i Plus spectrophotometer. The PL, PLE, PL decay and PLQY spectra at room temperature were acquired by an FS5 fluorescence spectrometer. The variable temperature spectrum was also collected by this spectrometer.

2.4. First principles calculations

All calculations in this study were performed with the Vienna *ab initio* Simulation Package (VASP)[32] within the frame of density functional theory (DFT). The exchange–correlation interactions of electron were described *via* the generalized gradient approximation (GGA) with PBE functional,[33] and the projector augmented wave (PAW) method[34] was used to describe the interactions of electron and ion. Additionally, the DFT-D3 method[35,36] was used to account for the long-range van der Waals forces present within the system. The Monkhorst–Pack scheme[37] was used for the integration in the irreducible Brillouin zone. The kinetic energy cut-off of 460 eV was chosen for the plane wave expansion. The lattice parameters and ionic position were fully relaxed, and the total energy was converged within 10–5 eV per formula unit. The final forces on all ions are less than 0.02/Å.

3 Results and discussion

Fig. 1a shows that the $(TMA)_2HfCl_6$ perovskite has a common cubic phase structure, in which each Hf^{4+} is coordinated with six Cl atoms to form $[HfCl_6]^{2-}$ octahedrons. Fig. 1b shows the powder X-ray diffraction (XRD) patterns for the $(TMA)_2HfCl_6$:Sb^{3+} samples. The peak positions gradually shift toward lower angles with increasing Sb^{3+} content, in accordance with the partial substitution of Hf^{4+} by the larger Sb^{3+} and indicating the successful incorporation of Sb^{3+} into the $(TMA)_2HfCl_6$ lattice.[38,39] Fig. 1c shows the Rietveld refinement of the XRD patterns of $(TMA)_2HfCl_6$:Sb^{3+}. The crystallographic data and structural parameters of $(TMA)_2HfCl_6$:Sb^{3+} are presented in Tables S1 and S2 (ESI†). Fig. S1 (ESI†) shows that the bond length of Hf–Cl is 2.477 Å and the bond angles of Cl–Hf–Cl are 89.47° and 90.53°. This result indicates an angular distortion in the octahedron, which induces different spatial orientations of the neighboring octahedrons. Fig. S2 (ESI†) shows the detailed crystal structure features of $(TMA)_2HfCl_6$:Sb^{3+}. Energy dispersive spectroscopy (EDS) elemental mapping indicates homogeneous distributions of Hf, Cl, and Sb in the $(TMA)_2HfCl_6$:Sb^{3+} crystals (Fig. 1d), demonstrating high phase purity. The $(TMA)_2HfCl_6$ and $(TMA)_2HfCl_6$:Sb^{3+}

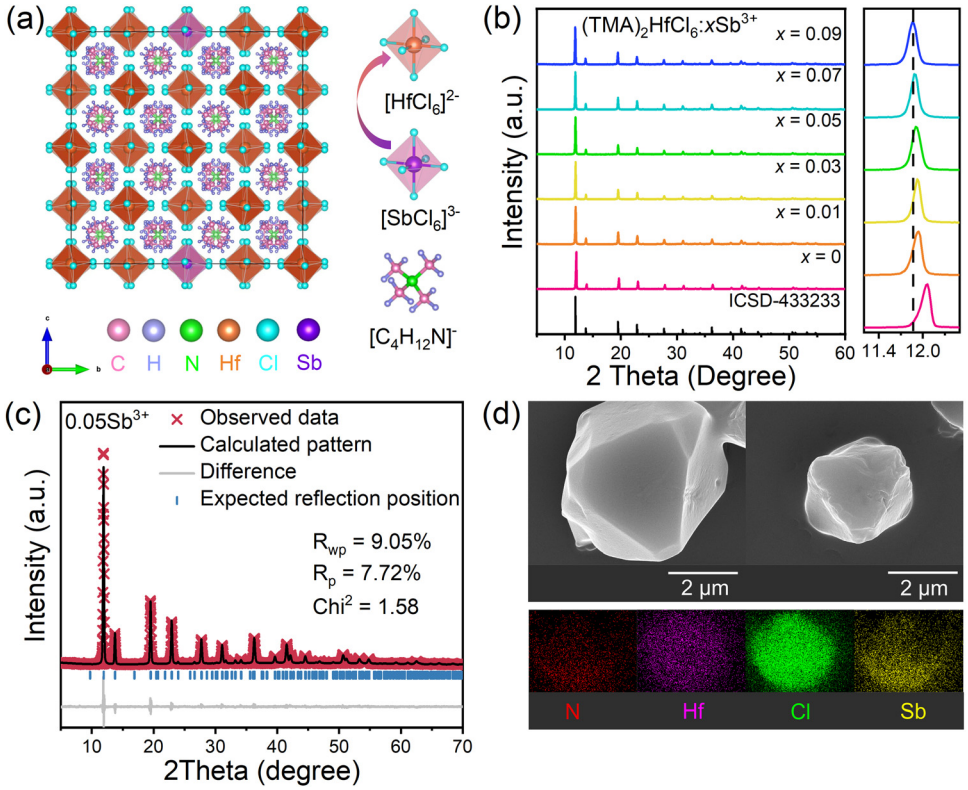

Fig. 1 (a) Schematic illustrations for the crystal structures of $(TMA)_2HfCl_6$ and Sb^{3+} doping $(TMA)_2HfCl_6$. (b) XRD patterns of $(TMA)_2HfCl_6$:Sb^{3+} with different Sb^{3+} doping concentrations. (c) Rietveld refinement of XRD patterns for TMA_2HfCl_6. (d) Energy-dispersive spectrometer (EDS) mapping of corresponding elements Hf, Sb, and Cl in $(TMA)_2HfCl_6$ and Sb^{3+} hybrid.

perovskites also exhibited excellent environmental stability. The PXRD of these samples remain unchanged after the sample was stored for 30 days in air (Fig. S3, ESI†). The sample exhibited good thermal stability, and the PL performance was almost unchanged upon increasing the sample temperature from room temperature to 450 K, as shown in Fig. S4 (ESI†).

To explore in detail the photophysical properties, the ultraviolet-visible (UV-vis) absorption spectra, as well as steady-state and time-resolved PL spectra were characterized. The $(TMA)_2HfCl_6$:Sb^{3+} crystals exhibited an additional broadband absorption in the UV regime, which was attributed to the incorporation of the Sb^{3+}-ion into the $(TMA)_2HfCl_6$ lattice (Fig. 2a). And their absorption intensity increased with increasing Sb^{3+} doping ratio. The Sb^{3+}-doped samples exhibited efficient broadband PL, whereas the undoped $(TMA)_2HfCl_6$ sample exhibited no visible PL. The PL intensity changed considerably with the concentration of the Sb^{3+} dopant. The feed concentration of Sb^{3+} ions should be fixed at 5% to optimize the PL intensity, because Sb^{3+} doping concentrations higher than 5% will cause concentration quenching that reduces the PL intensity (Fig. S5, ESI†).[40] The highest PLQY of the doping-induced emission was recorded as 85% (Fig. S6 and S7, ESI†), which is higher than Cs_2HfCl_6:Sb^{3+} (35.12%). Amazingly, Sb^{3+}-doped samples exhibit a unique excitation-dependent emission, covering a wide range of the visible light spectrum, as shown in Fig. 2c. The PL spectrum obtained under excitation from 280 to 350 nm contains two emission peaks centered at 490 and 660 nm. For excitation wavelengths exceeding 350 nm, there is no 490 nm emission in the PL spectrum. The intensity ratio of the two emission peaks in the PL spectrum changes with the excitation wavelength, such that the sample exhibits various luminescent colors (Fig. 2e). The intensity of the emission peak at 490 nm reaches a maximum under 310 nm excitation, and the sample emits bright white light with a CIE of (0.37, 0.36). At an excitation wavelength of 365 nm, the sample exhibits bright red luminescence with a high PLQY of up to 85.55%. Fig. 2b shows the PL excitation (PLE) spectra of the sample. The emission bands at 490 and 660 nm indicate there are different maximum excitation wavelengths for the two emission groups. The different PLE spectral profiles of the two emissions shown in Fig. 2b and d suggest there are different mechanisms for these two groups of emissions. Due to the significantly larger excitation range of the 660 nm emission band compared to the 490 nm emission band, therefore, dynamic color delivery of Sb^{3+}-doped samples can be obtained by accurate control of the excitation wavelength. This conclusion maintains efficient consistency with the above CIE results.

Time-resolved PL decay spectra of the sample were recorded to gain insight into the emission mechanisms (Fig. 2f–h). The lifetime monitored at 490 nm exhibits a single-exponential decay with a short component of 18.23 ns. Table S3 (ESI†) shows the lifetimes of different emission peaks under a 320 nm

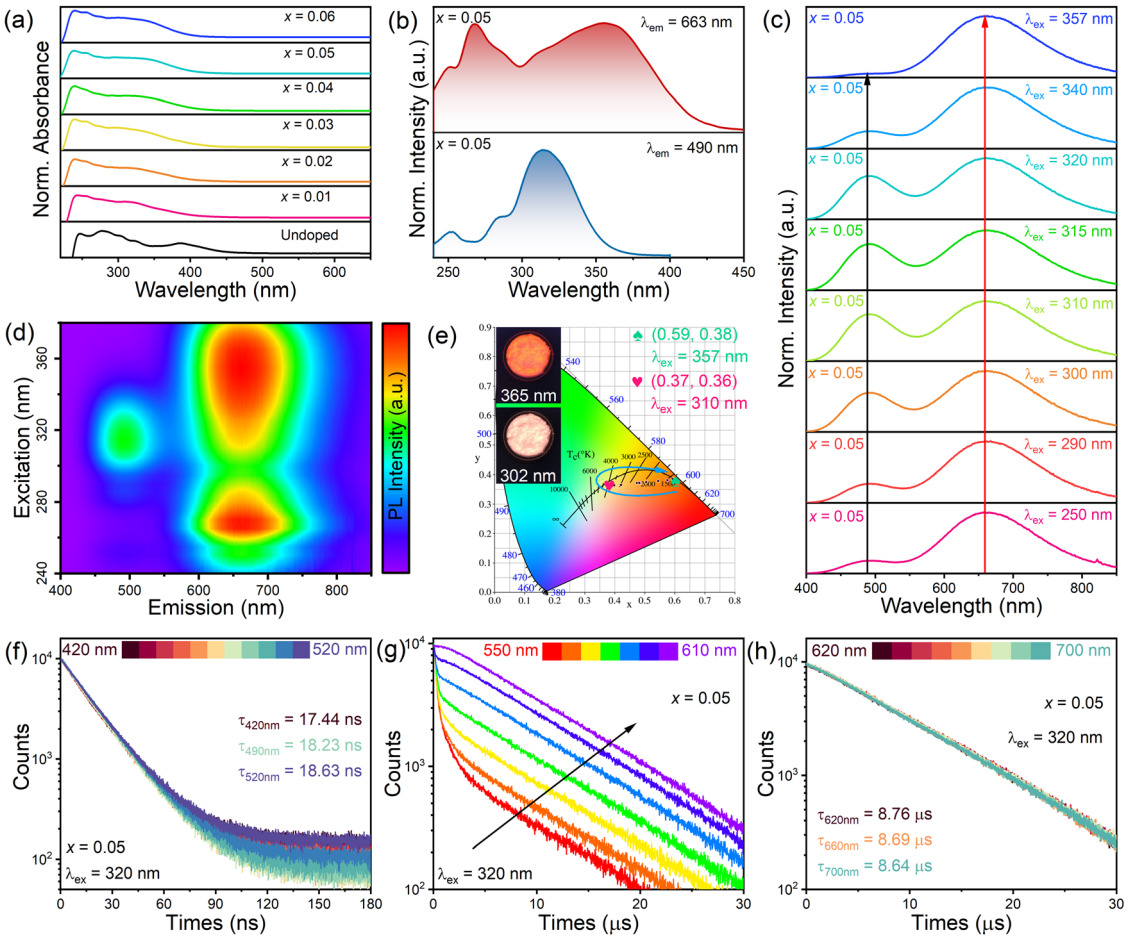

Fig. 2 (a) Absorption spectra of the $(TMA)_2HfCl_6$:xSb^{3+} (x = 0–0.06). (b) PL excitation (PLE) of 663 and 490 nm emission in $(TMA)_2HfCl_6$:0.05 Sb^{3+} crystals. (c) PL spectra of $(TMA)_2HfCl_6$: Sb^{3+} under different excitation wavelengths varying from 250 to 357 nm. (d) Contour plot of the excitation-dependent photoluminescence of the $(TMA)_2HfCl_6$:0.05 Sb^{3+} crystals. (e) The corresponding CIE color coordinates of the $(TMA)_2HfCl_6$:0.05 Sb^{3+} samples under different excitation wavelengths. (the inset are the photos of the as-prepared samples under different UV lamp). PL decay curves of $(TMA)_2HfCl_6$:0.05 Sb^{3+} in emission wavelength range of (f) 420–450 nm, (g) 550–610 nm, and (h) 620–700 nm excited by 320 nm.

excitation. The shortness of the lifetime suggests that the emission band at 490 nm could originate from FEs.[41] The lifetime monitored at 660 nm exhibits a slow decay with a long lifetime of 8.69 μs. On the basis of the microsecond-level long decay time and the observed large Stokes shift, the broadband emission at 660 nm can be reasonably inferred to originate from STEs.[42–44] In the wavelength range over which the fast and slow decays intersect (550–600 nm), the decay curves can be well-fitted by a biexponential decay process with two lifetimes (τ_{FE} and τ_{STE}, corresponding to the fast and slow decay processes). As the monitoring wavelength (550–600 nm) increases, the proportion of fast decay components decreases, while the proportion of slow decay components increases. This phenomenon suggests there are two independent PL components in the corresponding wavelength range.[45] In the high-energy (420–520 nm) or low-energy (620–700 nm) wavelength ranges, the decay curves show similar profiles as the emission wavelength changes. These results suggest that the high-energy PL component with a short lifetime and the low-energy PL component with a long lifetime can be attributed to the emission of FEs and STEs, respectively.

To better understand the photophysical mechanism, temperature-dependent PL spectra were recorded (Fig. 3) and used to analyze the exciton–phonon coupling. In the temperature-dependent PL spectra obtained under 320- and 357 nm excitations, the PL intensity increases as the temperature decreases. Fig. 3a shows there are two emission centers in $(TMA)_2HfCl_6$:Sb^{3+} at 150 K, corresponding to peaks at 490 and 660 nm in the PL spectrum, with more intense PL for the high-energy emission than the low-energy emission. This phenomenon provides further evidence that the two emissions correspond to the emission of FEs and STEs, respectively. The high-energy FE emission becomes less intense than the low-energy STE emission above 300 K. With increasing temperature, the intense lattice vibration weakens the FE emission considerably compared with the STE emission. Fig. 3a–c shows that as the temperature decreases, the emission peak at 490 nm increases in intensity and narrows, whereas the emission peak at 660 nm narrows and is shifted to the long-wavelength regime, which is consistent with a population transfer between STEs and FEs at low temperatures.[46] The temperature-dependent full width at half-maximum (FWHM) can be fit to determine the

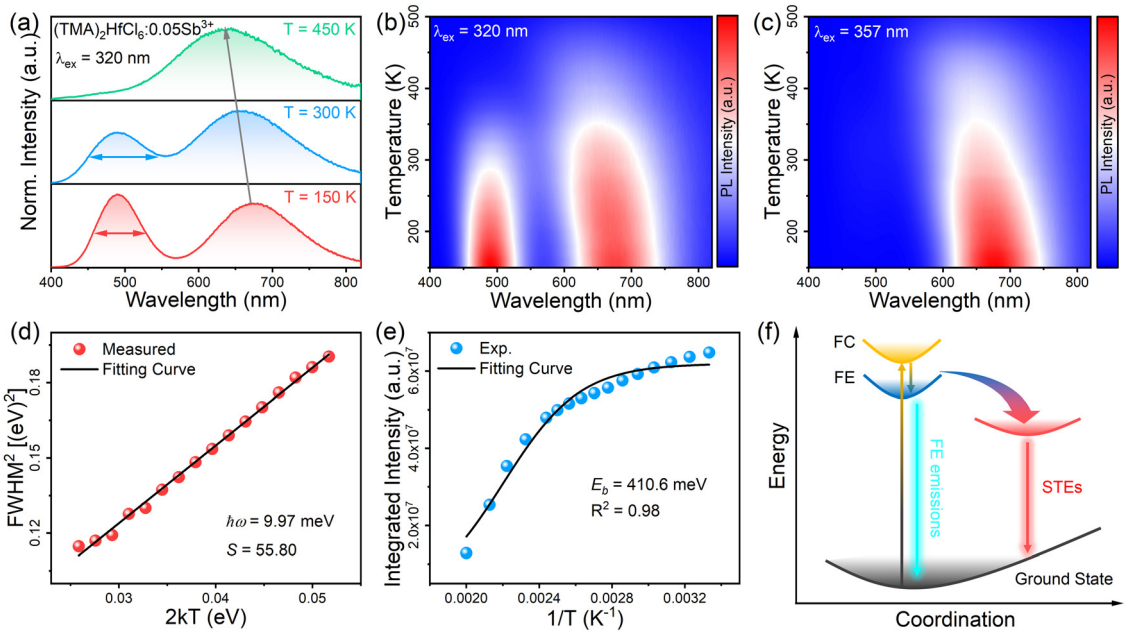

Fig. 3 (a) Normalized PL spectra of $(TMA)_2HfCl_6$:0.05 Sb^{3+} at 150 K, 300 K and 450 K. (b) Pseudo color mapping of temperature dependent PL spectra of $(TMA)_2HfCl_6$:0.05 Sb^{3+} under (b) 320 nm, and (c) 357 nm excitation. (d) Fitting results of the FWHM as a function of the temperature of $(TMA)_2HfCl_6$:0.05 Sb^{3+}. (e) Dependence of the PL intensity on 1/T of $(TMA)_2HfCl_6$:0.05 Sb^{3+}. (f) The configuration coordinate diagram demonstrating the photophysical process in $(TMA)_2HfCl_6:Sb^{3+}$.

Huang–Rhys factor (S), which reflects the electron–phonon coupling strength. The following equation relates S and FWHM:[47,48]

$$\mathrm{FWHM}(T) = 2.36\sqrt{S}\hbar\omega_{\mathrm{phonon}}\sqrt{\coth\frac{\hbar\omega_{\mathrm{phonon}}}{2k_{\mathrm{B}}T}} \quad (1)$$

where $\hbar\omega_{\mathrm{phonon}}$ denotes the phonon frequency and k_{B} denotes the Boltzmann constant. Fig. 3d shows that the as-prepared $(TMA)_2HfCl_6:Sb^{3+}$ sample has an S of 55.80, corresponding to strong electron–phonon coupling. Thus, the low-energy emission at 660 nm can be attributed to STE emission. The binding energy (E_b) of $(TMA)_2HfCl_6:Sb^{3+}$ can be fitted by the following function:[49,50]

$$I(T) = I_0/(1 + A\exp^{-E_b/k_BT}) \quad (2)$$

where I_0 is the integrated intensity at 0 K and A is a constant. Fig. 3e shows that E_b of $(TMA)_2HfCl_6:Sb^{3+}$ is determined to be 410.6 meV, which is considerably higher than the thermal energy at room temperature (~26 meV), indicating the formation of STEs that are stable to thermal decomposition.[51] Fig. 3f shows a PL mechanism for $(TMA)_2HfCl_6:Sb^{3+}$ proposed on the basis of the aforementioned results. Under a high-energy excitation, the electrons are excited to the free exciton excited state, manifesting as high-energy FE emission. Some of the electrons in the FE state can transfer to the STE state and then return to the ground state, producing broadband emission.

To further elucidate the optical properties, DFT calculations were performed to determine the electronic structures of the $(TMA)_2HfCl_6$ and $(TMA)_2HfCl_6:Sb^{3+}$ systems, which are shown in Fig. 4 and Fig. S8, and S9 (ESI†). In the pristine $(TMA)_2HfCl_6$ system, the conduction band minimum (CBM) is mainly composed of Cl p states and Hf d states and the valence-band maximum (VBM) mainly consists of Cl p orbitals (Fig. 4a and b). For $(TMA)_2HfCl_6$ doped with Sb, the CBM is composed of Cl p and Hf d orbitals and the VBM mainly consists of Sb s and Cl p orbitals (Fig. 4c and d). The organic component, $(TMA)^+$, of the lattice contributes negligibly to the VBM and CBM. Thus, the organic cations do not play an important role in the photophysical process in the Sb-doped $(TMA)_2HfCl_6$ system, and the optical properties of $(TMA)_2HfCl_6:Sb^{3+}$ mainly result from the electron transition in the inorganic metal halide species. The ground-state 5s Sb orbitals hybridized with the Cl 3p orbitals lie 1.45 eV above the host VBM, whereas the excited-state 5p Sb orbitals hybridized with the Cl 3p orbitals lie 0.72 eV above the host CBM. The gap between the excited and ground states of the $[SbCl_6]$ polyhedron is 3.80 eV, which is close to the energy of the PLE peak. These calculations confirm that the observed optical properties originate from the Sb^{3+} dopant. The isolated and extremely narrow bands near the CBM and VBM can facilitate charge localization and promote the formation of electron and hole polarons, which in turn trap excitons to form STEs.

4 Conclusions

In summary, we have reported remarkable excitation-dependent luminescence in $(TMA)_2HfCl_6:Sb^{3+}$ crystals, which enables efficient multicolor emission. On the basis of theoretical calculations and experimental characterizations (temperature-dependent steady-state PL spectra and lifetime decay curves), we attributed the origin of the dual emission at 490 and 660 nm to FEs and

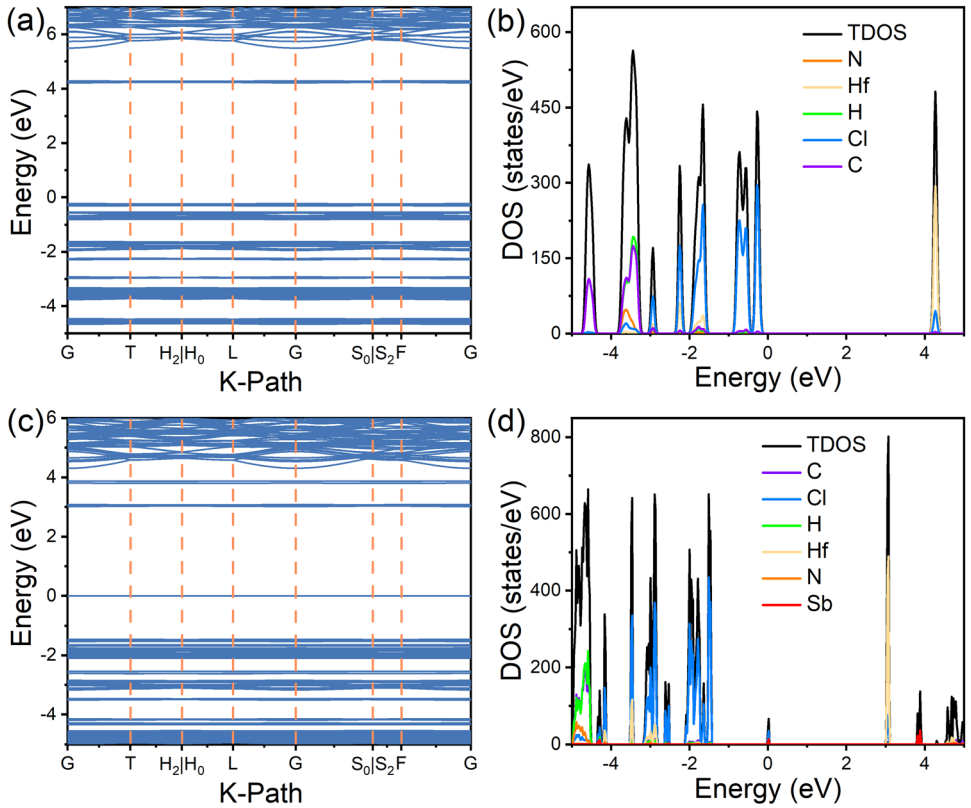

Fig. 4 DFT simulations. (a) electronic band structures and (b) density of states (DOS) of $(TMA)_2HfCl_6$; (c) electronic band structures and (d) DOS of Sb^{3+}-doped $(TMA)_2HfCl_6$.

STEs, respectively. The novel hybrid organic–inorganic Hf(IV) metal halide exhibits unique excitation-dependent emission under Sb^{3+} doping, that is, bright white emission under 310 nm excitation and bright red emission under 365 nm excitation. Thus, $(TMA)_2HfCl_6$:Sb^{3+} is a unique organic–inorganic metal halide that produces excitation-dependent colored emissions through two different light-emission modes. This property may provide useful insights for developing metal-halide luminescent materials.

Conflicts of interest

There are no conflicts to declare.

Acknowledgements

Y. S. acknowledges the support from the National Natural Science Foundation of China (Grant No. 61874074) and Science and Technology Project of Shenzhen (Grant No. JCYJ20220531100815034). H. L. acknowledges the support from Guangdong Basic and Applied Basic Research Foundation (General Program, Grant No. 2022A1515012055).

References

1 C. K. Zhou, Y. Tian, O. Khabou, M. Worku, Y. Zhou, J. Hurley, H. R. Lin and B. W. Ma, Manganese-Doped One-Dimensional Organic Lead Bromide Perovskites with Bright White Emissions, *ACS Appl. Mater. Interfaces*, 2017, **9**, 40446–40451.

2 Z. Yuan, C. K. Zhou, Y. Tian, Y. Shu, J. Messier, J. C. Wang, L. J. Burgt, K. Kountouriotis, Y. Xin, E. Holt, K. Schanze, R. Clark, T. Siegrist and B. W. Ma, One-dimensional organic lead halide perovskites with efficient bluish white-light emission, *Nat. Commun.*, 2017, **8**, 14051.

3 J. W. Lin, M. W. Zhang, N. Sun, S. H. He, X. S. Zhang, Z. N. Guo, J. Zhao, Q. L. Liu and W. X. Yuan, Narrowing the band of green emission in manganese hybrids by reducing the hydrogen bond strength and structural distortion, *J. Mater. Chem. C*, 2022, **10**, 16773–16780.

4 D. Y. Li, Y. M. Sun, X. Y. Wang, N. N. Wang, X. Y. Zhang, C. Y. Yue and X. W. Lei, Zero-Dimensional Hybrid Indium Halides with Efficient and Tunable White-Light Emissions, *J. Phys. Chem. Lett.*, 2022, **13**, 6635–6643.

5 B. B. Su and Z. G. Xia, Research Progresses of Photoluminescence and Application for Emerging Zero-dimensional Metal Halides Luminescence Materials, *Chin. J. Lumin.*, 2021, **42**, 733–754.

6 S. Q. Sun, M. Lu, X. P. Gao, Z. F. Shi, X. Bai, W. W. Yu and Y. Zhang, 0D Perovskites: Unique Properties, Synthesis, and Their Applications, *Adv. Sci.*, 2021, **8**, 2102689.

7 Y. L. Jiang and H. H. Fei, Efficient and Stable Self-Trapped Blue Emission from a 1D Organolead Chloride Crystalline Material, *Adv. Opt. Mater.*, 2022, **10**, 2102148.

8 P. G. Han, C. Luo, S. Q. Yang, Y. Yang, W. Q. Deng and K. L. Han, All-Inorganic Lead-Free 0D Perovskites by a Doping Strategy to Achieve a PLQY Boost from <2% to 90%, *Angew. Chem., Int. Ed.*, 2020, **59**, 12709–12713.

9 B. Zhou, Z. X. Liu, H. N. Li, S. F. Fang, F. E. Fang, Y. Wang, F. M. Chen and Y. M. Shi, Highly Efficient White-Light Emission Triggered by Sb^{3+} Dopant in Indium-Based Double Perovskites, *Adv. Photonics Res.*, 2021, **2**, 2100143.

10 Y. Y. Jing, Y. Liu, J. Zhao and Z. G. Xia, Sb^{3+} Doping-Induced Triplet Self-Trapped Excitons Emission in Lead-Free Cs_2SnCl_6 Nanocrystals, *J. Phys. Chem. Lett.*, 2019, **10**, 7439–7444.

11 K. Han, J. W. Qiao, S. Zhang, B. B. Su, B. B. Lou, C. G. Ma and Z. G. Xia, Band Alignment Engineering in ns^2 Electrons Doped Metal Halide Perovskites, *Laser Photonics Rev.*, 2022, **17**, 2200458.

12 X. Y. Shi, Z. L. Li, M. Y. Cao, Z. H. Rao, X. J. Zhao and X. Gong, Fast HCl-free Synthesis of Lead-free Rb_2ZrCl_6:$x$$Sb^{3+}$ Perovskites, *Inorg. Chem.*, 2022, **61**, 14095–14101.

13 S. P. Liu, B. Yang, J. S. Chen, D. Y. Zheng, Z. Tang, W. Q. Deng and K. L. Han, Colloidal Synthesis and Tunable Multicolor Emission of Vacancy-Ordered Cs_2HfCl_6 Perovskite Nanocrystals, *Laser Photonics Rev.*, 2022, **16**, 2100439.

14 J. H. Li, Z. F. Tan, M. C. Hu, C. Chen, J. J. Luo, S. R. Li, L. Gao, Z. W. Xiao, G. D. Niu and J. Tang, Antimony doped Cs_2SnCl_6 with bright and stable emission, *Front. Optoelectron.*, 2019, **12**, 352–364.

15 G. D. Zhang, P. P. Dang, H. Xiao, H. Z. Lian, S. Liang, L. Yang, Z. Y. Cheng, G. G. Li and J. Lin, Antimony-Doped Lead-Free Zero-Dimensional Tin(IV)-Based Organic–Inorganic Metal Halide Hybrids with High Photoluminescence Quantum Yield and Remarkable Stability, *Adv. Opt. Mater.*, 2021, **9**, 2101637.

16 G. Yang, S. C. Bai, X. G. Li, H. Liang, C. Li, J. Sun, Y. H. Wang, J. S. Huang, G. C. Pan and Y. S. Zhu, Tunable and Efficient Photoluminescence of Lanthanide-Doped $Cs_2NaScCl_6$ Double Perovskite Single Crystals toward Multifunctional Light-Emitting Diode Applications, *ACS Appl. Mater. Interfaces*, 2023, **15**, 24629–24637.

17 H. W. Li, M. L. Zhang, Y. Li, X. Y. Fu, J. Feng and H. J. Zhang, Efficient Multi-Luminescence Covering the Visible to Near-Infrared Range in Antimony and Lanthanide Co-Doped Indium-Based Zero-Dimensional Perovskites Nanocrystals, *Adv. Opt. Mater.*, 2023, **11**, 2300429.

18 W. G. Huang, H. Peng, Q. L. Wei, J. J. Xia, X. F. He, B. Ke, Y. Tian and B. S. Zou, Tunable Efficient White Emission in Holmium Doped Double Perovskites Cs_2KInCl_6 via Antimony Sensitization, *Adv. Opt. Mater.*, 2023, **11**, 2203103.

19 W. Yang, P. P. Dang, G. D. Zhang, H. Z. Lian, Z. Y. Cheng, G. G. Li and J. Lin, Mn^{2+} as an "Optical Energy Shutter" to Regulate Red-to-NIR Luminescence in Rare Earth Doped Layered Quadruple Perovskites, *Adv. Opt. Mater.*, 2023, 2300468.

20 S. R. Li, Q. S. Hu, J. J. Luo, T. Jin, J. Liu, J. H. Li, Z. F. Tan, Y. B. Han, Z. Zheng, T. Y. Zhai, H. S. Song, L. Gao, G. D. Niu and J. Tang, Self-Trapped Exciton to Dopant Energy Transfer in Rare Earth Doped Lead-Free Double Perovskite, *Adv. Opt. Mater.*, 2019, **7**, 1901098.

21 Y. Liu, M. L. Zaffalon, J. Zito, F. Cova, F. Moro, M. Fanciulli, D. X. Zhu, S. Toso, Z. G. Xia, I. Infante, L. D. Trizio, S. Brovelli and L. Manna, $Cu^{+} \rightarrow Mn^{2+}$ Energy Transfer in Cu, Mn Coalloyed Cs_3ZnCl_5 Colloidal Nanocrystals, *Chem. Mater.*, 2022, **34**, 8603–8612.

22 X. Y. Liu, X. Xu, B. Li, Y. Q. Liang, Q. Li, H. Jiang and D. S. Xu, Antimony-Doping Induced Highly Efficient Warm-White Emission in Indium-Based Zero-Dimensional Perovskites, *CCS Chem.*, 2020, **2**, 216–224.

23 A. Noculak, V. Morad, K. M. McCall, S. Yakunin, Y. Shynkarenko, M. Wörle and M. V. Kovalenko, Bright Blue and Green Luminescence of Sb(III) in Double Perovskite Cs_2MInCl_6 (M = Na, K) Matrices, *Chem. Mater.*, 2020, **32**, 5118–5124.

24 Y. P. Fu, S. Jin and X. Y. Zhu, Stereochemical expression of ns^2 electron pairs in metal halide perovskites, *Nat. Rev. Chem.*, 2021, **5**, 838–852.

25 Z. Jia, P. F. Gong, J. Zhao, M. X. Chen, Y. G. Wang, Z. G. Wang, Y. Dong and M. J. Xia, Antimony-doped enhanced photoluminescence quantum yield in zero-dimensional lead-free metal halide $Rb_2CsBiCl_6$ crystals, *Inorg. Chem. Front.*, 2022, **9**, 6299–6304.

26 S. F. Wu, W. B. Li, J. J. Hu and P. Gao, Antimony doped lead-free double perovskites ($Cs2NaBi_{1-x}Sb_xCl_6$) with enhanced light absorption and tunable emission, *J. Mater. Chem. C*, 2020, **8**, 13603–13611.

27 Y. Guo, J. K. Chen, B. Chen, W. L. Zheng, X. Zhang, H. Suo, F. J. Chun, X. H. Wei and F. Wang, Sequential thermochromic switching in zero-dimensional Cs_2ZnCl_4 metal halides, *Mater. Today Phys.*, 2023, **35**, 101111.

28 Z. Y. Li, Y. Li, P. Liang, T. L. Zhou, L. Wang and R. J. Xie, Dual-Band Luminescent Lead-Free Antimony Chloride Halides with Near-Unity Photoluminescence Quantum Efficiency, *Chem. Mater.*, 2019, **31**, 9363–9371.

29 J. Zhou, M. Z. Li, M. S. Molokeev, J. Y. Sun, D. H. Xu and Z. G. Xia, Tunable photoluminescence in Sb^{3+}-doped zero-dimensional hybrid metal halides with intrinsic and extrinsic self-trapped excitons, *J. Mater. Chem. C*, 2020, **8**, 5058–5063.

30 X. Li, X. P. Gao, X. T. Zhang, X. Y. Shen, M. Lu, J. L. Wu, Z. F. Shi, V. L. Colvin, J. H. Hu, X. Bai, W. W. Yu and Y. Zhang, Lead-Free Halide Perovskites for Light Emission: Recent Advances and Perspectives, *Adv. Sci.*, 2021, **8**, 2003334.

31 B. Chen, Y. Guo, Y. Wang, Z. Liu, Q. Wei, S. X. Wang, A. L. Rogach, G. C. Xing, P. Shi and F. Wang, Multiexcitonic Emission in Zero-Dimensional Cs_2ZrCl_6:Sb^{3+} Perovskite Crystals, *J. Am. Chem. Soc.*, 2021, **143**, 17599–17606.

32 G. Kresse and J. Furthmuller, Efficient Iterative Schemes for Ab Initio Total-Energy calculations Using a Plane-Wave Basis Set, *Phys. Rev. B: Condens. Matter Mater. Phys.*, 1996, **54**, 11169–11186.

33 J. P. Perdew, K. Burke and M. Ernzerhof, Generalized gradient approximation made simple, *Phys. Rev. Lett.*, 1996, **77**, 3865–3868.

34 G. Kresse and J. Joubert, From Ultrasoft Pseudopotentials to the Projector Augmented-Wave Method, *Phys. Rev. B: Condens. Matter Mater. Phys.*, 1999, **59**, 1758–1775.

35 S. Grimme, J. Antony, S. Ehrlich and H. Krieg, A consistent and accurate ab initio parametrization of density functional dispersion correction (DFT-D) for the 94 elements H-Pu, *J. Chem. Phys.*, 2010, **132**, 154104.
36 S. Grimme, S. Ehrlich and L. Goerigk, Effect of the damping function in dispersion corrected density functional theory, *J. Comput. Chem.*, 2011, **32**, 1211–1491.
37 H. J. Monkhorst and J. D. Pack, Special points for Brillouin-zone integrations, *Phys. Rev. B: Solid State*, 1976, **13**, 5188–5192.
38 J. H. Nie, H. N. Li, S. F. Fang, B. Zhou, Z. X. Liu, F. M. Chen, Y. Wang and Y. M. Shi, Efficient red photoluminescence in holmium-doped $Cs_2NaInCl_6$ double perovskite, *Cell Rep. Phys. Sci.*, 2022, **3**, 100820.
39 L. K. Wu, R. F. Li, W. Y. Wen, Q. H. Zou, H. Y. Ye and J. R. Li, Lead-free hybrid indium perovskites with near-unity PLQY and white light emission using an Sb^{3+} doping strategy, *Inorg. Chem. Front.*, 2023, **10**, 3297–3306.
40 R. S. Zeng, K. Bai, Q. L. Wei, T. Chang, J. Yan, B. Ke, J. L. Huang, L. S. Wang, W. C. Zhou, S. Cao, J. L. Zhao and B. S. Zou, Boosting triplet self-trapped exciton emission in Te(IV)-doped Cs_2SnCl_6 perovskite variants, *Nano Res.*, 2020, **14**, 1551–1558.
41 B. Zhou, Z. X. Liu, S. F. Fang, J. H. Nie, H. Z. Zhong, H. L. Hu, H. N. Li and Y. M. Shi, Emission Mechanism of Self-Trapped Excitons in Sb^{3+}-Doped All-Inorganic Metal-Halide Perovskites, *J. Phys. Chem. Lett.*, 2022, **13**, 9140–9147.
42 C. Fang, Y. J. Mao, G. J. Zhou, Z. C. Zhang, Y. H. Zhu, D. H. Xu, X. Li, A. C. Geng and J. Zhou, Zero-dimensional indium hybrids and modulated photoluminescence by Sb doping, *Mater. Chem. Front.*, 2023, **7**, 3164–3171.
43 Z. L. Li, Q. Q. Li, M. Y. Cao, Z. H. Rao, X. Y. Shi, L. J. Zhou, X. J. Zhao and X. Gong, Multimodal Luminescent Low-Dimension Cs_2ZrCl_6:$x$$Sb^{3+}$ Crystals for White Light-Emitting Diodes and Information Encryption, *Langmuir*, 2023, **39**, 3792–3799.
44 H. Arfin and A. Nag, Origin of Luminescence in Sb^{3+}-and Bi^{3+}-Doped Cs_2SnCl_6 Perovskites: Excited State Relaxation and Spin-Orbit Coupling, *J. Phys. Chem. Lett.*, 2021, **12**, 10002–10008.
45 P. F. Fu, S. N. Geng, R. X. Mi, R. Y. Wu, G. Y. Zheng, B. B. Su, Z. G. Xia, G. D. Niu, J. Tang and Z. W. Xiao, Achieving Narrowed Bandgaps and Blue-Light Excitability in Zero-Dimensional Hybrid Metal Halide Phosphors via Introducing Cation-Cation Bonding, *Energy Environ. Mater.*, 2022, **0**, e12518.
46 R. L. Zhang, X. Mao, Y. Yang, S. Q. Yang, W. Y. Zhao, T. Wumaier, D. H. Wei, W. Q. Deng and K. L. Han, Air-Stable, Lead-Free Zero-Dimensional Mixed Bismuth-Antimony Perovskite Single Crystals with Ultra-broadband Emission, *Angew. Chem., Int. Ed.*, 2019, **58**, 2725–2729.
47 Y. L. Gao, Q. L. Wei, T. Chang, M. Ren, Y. F. Lou, Z. J. Tian, Y. Fan, J. D. Yao, B. S. Zou and R. S. Zeng, Highly efficient warm white light emission in Sb^{3+}-doped $(NH_4)_4CdCl_6$ metal halides through A-site Rb-alloying regulation, *J. Mater. Chem. C*, 2023, **11**, 8486–8494.
48 Y. H. Chen, L. Zhou, S. G. Zhou, D. H. You, H. Z. Xiong, Y. H. Hu, Q. L. Chen, R. X. He and M. Li, Effect of the Host Lattice Environment on the Expression of $5s^2$ Lone-Pair Electrons in a 0D Bismuth-Based Metal Halide, *Inorg. Chem.*, 2023, **62**, 2806–2816.
49 S. F. Fang, H. N. Li, Y. L. Xie, H. X. Li, Y. Wang and Y. M. Shi, Zero-Dimensional Organic-Inorganic Hybrid Copper-Based Halides with Highly Efficient Orange-Red Emission, *Small*, 2021, **17**, 2103831.
50 J. H. Nie, B. Zhou, S. F. Fang, Y. Wang, Y. Wang, B. B. Tian, H. L. Hu, H. Z. Zhong, H. N. Li and Y. M. Shi, Chemical doping of lead-free metal-halide-perovskite related materials for efficient white-light photoluminescence, *Mater. Today Phys.*, 2023, **31**, 100992.
51 Q. L. Wei, X. F. Meng, W. C. Lin, S. G. Ge, X. X. Han, L. Chen, R. S. Zeng and B. S. Zou, Green Triplet Self-Trapped Exciton Emission in Layered $Rb_3Cd_2Cl_7$:Sb^{3+} Perovskite: Comparison with $RbCdCl_3$:Sb^{3+}, *J. Phys. Chem. Lett.*, 2022, **13**, 8436–8446.